

Magnon Kerr effect in a magnetic thin film strongly coupled to a microwave resonator

Davit Petrosyan,^{1,*} Hiroki Matsumoto,^{1,2} Hanchen Wang,¹ Jamal Ben Youssef,³ Richard Schlitz,⁴ William Legrand,^{1,5,†} and Pietro Gambardella^{1,‡}

¹*Department of Materials, ETH Zurich, CH-8093 Zurich, Switzerland*

²*Institute for Chemical Research, Kyoto University, 6110011 Uji, Japan*

³*LabSTICC, CNRS, Université de Bretagne Occidentale, 29238 Brest, France*

⁴*Department of Physics, University of Konstanz, 78457 Konstanz, Germany*

⁵*Université Grenoble Alpes, CNRS, Institut Néel, 38042 Grenoble, France*

Cavity magnonics investigates hybrid systems where magnons interact coherently with photons, providing a platform to harness light–matter interaction in magnetic materials. Progress in this field hinges on achieving stronger and tunable nonlinear effects, which are essential for controlling magnon dynamics and frequency conversion. Here, we demonstrate the magnon Kerr effect in an anisotropic magnonic system comprising a 200 nm-thick yttrium iron garnet film strongly coupled to a three-dimensional microwave resonator. The strong shape anisotropy significantly enhances the magnon Kerr effect compared to a sphere of equivalent volume, while the cavity enables sensitive probing of magnetization dynamics. We demonstrate continuous tunability of the magnitude and sign of the Kerr shift by controlling the static orientation of the magnetization. Input-output modeling of the magnon–photon interaction provides a consistent description of our system and Kerr coefficients matching the experimental results. Our findings demonstrate a scalable approach to enhancing Kerr anharmonicity in hybrid magnon–photon systems while preserving strong coupling.

The field of cavity magnonics explores interactions between exchange-coupled electronic spins in magnetically ordered materials and microwave photons in electromagnetic resonators [1–4]. First demonstrated in experiments with single-crystal yttrium iron garnet (YIG) spheres [5, 6], this concept has been extended to the ultra-strong coupling regime [6–8], planar cavities [7, 9–11], and integrated devices [12–14]. By combining ferromagnetic resonance modes with cavity electrodynamics, strong magnon–photon coupling enables highly sensitive spectral probing of magnon dynamics. The field confinement inside the cavity enhances the effective drive strength and prevents radiative decay, allowing for large magnon populations. This facilitates the exploration of nonlinear magnon regimes, where magnon–magnon interactions modify their collective response to microwave excitation [15–18].

Among magnon nonlinearities, the magnon Kerr effect (MKE) appears in all ferromagnets with finite magnetic anisotropy, manifesting as a self-induced frequency shift of the magnon modes. Unlike other nonlinear effects, the MKE does not require external parametric pumping [19–22], or any dispersion matching as in three-magnon scattering [15, 23–29]. The MKE has been demonstrated in cavity-coupled YIG spheres [30], where it gives rise to bistability of magnon–polaritons [31]. Moreover, Kerr nonlinearities can also arise between magnons and other bosonic quasi-particles [32–34] under sufficient populations of the respective modes. The MKE is hence a direct and desirable approach for inducing magnon nonlinearities [35–39] and entangle different degrees of freedom in hybrid systems [40–42].

In general, the MKE can be enhanced by reducing the volume of the magnonic system, or by increasing its mag-

netic anisotropy. This sets a limit to the MKE that can be achieved with YIG spheres, due to the lower bound on their volumes (diameter > 0.2 mm) and their inherently small magnetocrystalline anisotropy. Confined magnets strongly coupled to superconducting resonators [12–14] provide an alternative solution, with magnetic volumes that are several orders of magnitude smaller. However, the nonlinearity of the superconducting resonators makes it difficult to disentangle the MKE from the cavity response [12]. These limitations motivate alternative approaches combining a three-dimensional (3D) or a planar harmonic resonator with a thin magnetic film [34, 43], which can simultaneously enhance the MKE while maintaining a linear photonic probing.

In this letter, we report the MKE in a YIG thin film strongly coupled to a 3D microwave cavity. The thin film geometry, combining reduced volume and strong shape anisotropy, significantly enhances the MKE compared to the smallest YIG spheres. We quantify the MKE from shifts of the magnon–polariton frequencies with varying microwave drive power. By changing the external field angle, we demonstrate continuous tunability of the strength and a sign change of the Kerr shift. We find excellent agreement between the Kerr coefficients extracted from our experiments and theoretical predictions. These results establish the MKE in magnetic thin films as a powerful tool to tune the properties of nonlinear magnonic systems.

The experimental setup is schematically shown in Fig. 1(a). A loop-gap resonator [Fig. 1(b)] is used to couple to the YIG film. A 200 nm-thick film of YIG was grown on both sides of a gadolinium gallium garnet (GGG) substrate by liquid phase epitaxy, after which one side was polished away. The film was cut to $2.5 \times 3.5 \text{ mm}^2$

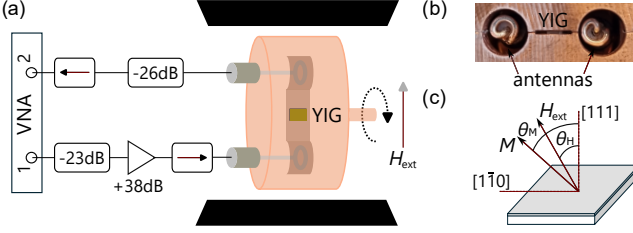


FIG. 1. (a) Experimental setup showing the sample and microwave resonator placed in an electromagnet and connected to the VNA. The microwave signal is amplified by net 15 dB. The resonator can be rotated to change the relative angle between the applied magnetic field and the sample plane. (b) Photograph of the resonator [44], with probing antennas and the YIG film in the sample space. (c) Schematic of field angle θ_H and magnetization angle θ_M with respect to the normal to the (111)-oriented YIG film.

and inserted into a loop-gap resonator [Fig. 1(b)] placed in the variable uniform magnetic field of an electromagnet, at room temperature. The loop-gap cavity design is described in Ref. 44. The orientation of the external field $\mu_0 H_{\text{ext}}$ relative to the sample plane is set by rotating the cavity. The microwave magnetic field in the resonator is always orthogonal to the static field, allowing for measurements through all intermediate angles between in-plane (IP) and out-of-plane (OOP) configurations. The angles θ_H and θ_M refer to the applied external field and magnetization, respectively [Fig. 1(c)]. Two ports of the resonator are connected to a vector network analyzer (VNA) to probe microwave transmission via the S_{21} scattering matrix term. The VNA signal is amplified to perform measurements at net powers incident on the cavity resonator, P , varying from -5 dBm to 25 dBm .

First, we measure $|S_{21}|$ in the IP configuration at $P = -5 \text{ dBm}$, for which a colormap encoding the transmission as a function of magnetic field and microwave frequency is presented in Fig. 2(a). The map features the avoided crossing between the cavity resonance and the Kittel mode, corresponding to the hybridized magnon–photon polariton modes. The same measurement for OOP field at $P = -5 \text{ dBm}$ is shown in Fig. 2(b). We find the magnon–photon coupling constant $g/(2\pi) = 35.9 \text{ MHz}$, total cavity linewidth $\kappa_{\text{tot}}/(2\pi) = 32.0 \text{ MHz}$, and magnon dissipation rates $\kappa_m/(2\pi) = 5.5 \text{ MHz}$ and 15.4 MHz for IP and OOP fields, respectively, from fits described in Supplemental Material (SM) [45]. We see that $g > \kappa_{\text{tot}}, \kappa_m$ in both configurations, sufficient to attain the strong-coupling regime. The present value for g is comparable to that obtained in previous works using bulk YIG spheres, despite those spheres having a total number of spins several orders of magnitude larger [30]. The cooperativity $g^2/(\kappa_{\text{tot}} \kappa_m)$, quantifying the overall coherence of the hybridization, is 7.3 and 2.6 for IP and OOP fields, respectively. The increase in κ_m for OOP field is due to inhomogeneous broadening [51].

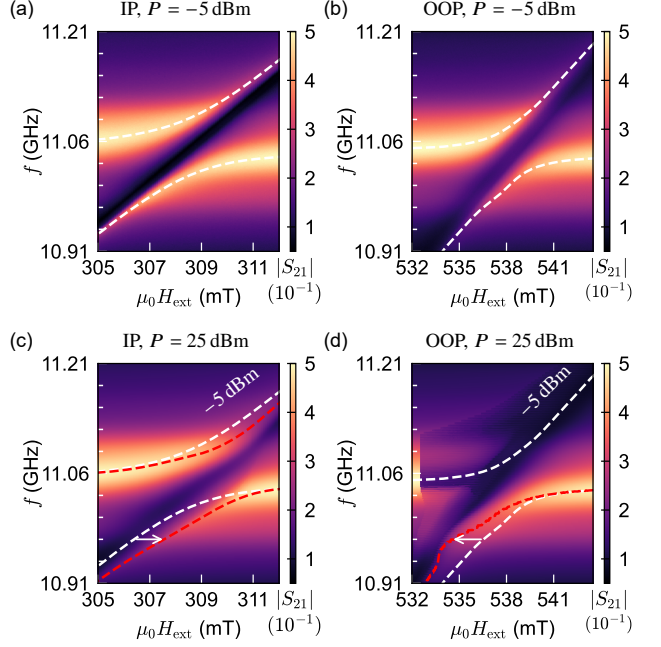


FIG. 2. Field- and frequency-dependent microwave transmission of the coupled magnon–photon system: measured in the IP configuration at (a) $P = -5 \text{ dBm}$ and (c) $P = 25 \text{ dBm}$, and in the OOP configuration at (b) $P = -5 \text{ dBm}$ and (d) $P = 25 \text{ dBm}$. Dashed lines follow the maximas in the transmission and mark the magnon–polariton branches at $P = -5 \text{ dBm}$ (white) and at $P = 25 \text{ dBm}$ (red), and arrows indicate the shift direction. The OOP upper magnon–polariton branch at $P = 25 \text{ dBm}$ does not appear due to foldover.

The hybrid modes are then measured at $P = 25 \text{ dBm}$. For IP field [Fig. 2(c)], the two polariton branches have shifted to higher fields (i.e., lower magnon frequencies), as visible by comparing the transmission maxima (red) and the reference (white) taken from Fig. 2(a). For OOP field [Fig. 2(d)], the lower branch has shifted in the opposite direction, to lower fields (i.e., higher magnon frequencies). These power-dependent shifts of the magnon–polariton branches are the signatures of the MKE in the system. The OOP measurement at $P = 25 \text{ dBm}$ also reveals a marked foldover effect of the resonance [16, 18], characterized by sharp changes in the transmission of the upper branch near 533 mT .

For further analysis, we measure the cavity transmission $|S_{21}|$ against frequency, keeping a constant magnetic field near the center of the avoided crossing. This allows us to record shifts of the two polariton peaks, while varying the power in fine steps. Figure 3(a) shows the measurements for IP field ($\theta_H = 90^\circ$). At high powers, the magnon–polariton peaks shift to lower frequencies. The shift is more apparent in the lower branch, which has a higher magnon character than the upper branch at high powers [46]. The measurement for OOP field ($\theta_H = 0^\circ$) is shown in Fig. 3(b), which corresponds to

a shift in the opposite direction. Moreover, at 15 dBm and above, oscillations with a periodicity of 3.2 MHz appear, corresponding to standing bulk acoustic modes in the YIG/GGG stack [52].

The sign reversal between the IP and OOP Kerr shifts suggests that at an intermediate angle, the MKE should be suppressed. We identify the angle where the MKE cancels by performing measurements similar to that in Fig. 3(a), with 5° steps, from IP to OOP configurations. Figure 3(c) shows the measurement at $\theta_H = 40^\circ$, where the magnon–polariton peaks do not shift in frequency with power. However, the amplitude of the transmission decreases with increasing power, attributed to an enhanced power-dependent damping in the YIG film, originating from nonlinear magnon scattering [45].

To describe and quantitatively determine the frequency shift due to the MKE for the magnon–polariton branches in a ferromagnetic thin film, we consider the following Hamiltonian for the coupled magnon–photon system [46]:

$$\hat{H}/\hbar = \omega_c \hat{c}^\dagger \hat{c} + \omega_m \hat{m}^\dagger \hat{m} + g(\hat{c}^\dagger \hat{m} + \hat{c} \hat{m}^\dagger) + \mathcal{K} \hat{m}^\dagger \hat{m} \hat{m}^\dagger \hat{m}, \quad (1)$$

where ω_c and ω_m are angular frequencies of the cavity and Kittel mode, respectively, \hat{c}^\dagger (\hat{c}) are the creation (annihilation) operators of the cavity mode, \hat{m}^\dagger (\hat{m}) are the creation (annihilation) operators of the Kittel mode, \mathcal{K} is the Kerr coefficient, and \hbar is the reduced Planck's constant. We use the mean field approximation for the quadratic term, similar to previous studies [30, 31], and obtain

$$\hat{H}/\hbar = \omega_c \hat{c}^\dagger \hat{c} + (\omega_m + 2\mathcal{K} \langle \hat{m}^\dagger \hat{m} \rangle) \hat{m}^\dagger \hat{m} + g(\hat{c}^\dagger \hat{m} + \hat{c} \hat{m}^\dagger). \quad (2)$$

Here, $\langle \hat{m}^\dagger \hat{m} \rangle$ is the expectation value for the magnon population and the term $2\mathcal{K} \langle \hat{m}^\dagger \hat{m} \rangle$ acts as a modulation of the magnon angular frequency, which induces the magnon–polariton shift.

The equations of motion of this Hamiltonian combined with input-output formalism provide a model for S_{21} [46], which we use to fit the experimental data [45]. Figure 3(d) and (e) show the fits to the data at $\theta_H = 90^\circ$ and $\theta_H = 0^\circ$, respectively, from which we obtain $\mathcal{K}_{\text{IP}}/(2\pi) = -57.7 \pm 0.9 \text{ nHz}$ and $\mathcal{K}_{\text{OOP}}/(2\pi) = 170 \pm 20 \text{ nHz}$. At $P = 25 \text{ dBm}$, the number of magnons in the system is of the order of 10^{14} . We limit the fit for OOP field at 11 dBm to avoid the foldover regime and magnon–phonon coupling present at higher powers, which cannot be analyzed by our input-output model. This quantitative analysis confirms that with increasing drive power, the peaks shift in opposite directions for IP and OOP magnetizations. Finally, Fig. 3(f) shows the fit at $\theta_H = 40^\circ$, from which we obtain $\mathcal{K}/(2\pi) = -3.1 \pm 0.8 \text{ nHz}$, highlighting the near cancellation of the MKE. We now compare these results to theoretical values.

The Kerr coefficients for a thin film magnetized IP and OOP are given by

$$\mathcal{K}_{\text{IP}} = \xi \frac{\hbar \gamma^2 K_u^*}{2 M_s^2 V_m}, \quad \mathcal{K}_{\text{OOP}} = -\frac{\hbar \gamma^2 K_u^*}{M_s^2 V_m}, \quad (3)$$

where γ is the gyromagnetic ratio, K_u^* the effective anisotropy constant (including contributions from uniaxial anisotropy mechanisms along the growth direction and shape anisotropy), M_s the saturation magnetization, V_m the volume of the film, $\xi = (B_{\text{eff}}/4 + \mu_0 H_{\text{ext}})/(B_{\text{eff}} + \mu_0 H_{\text{ext}}) = 0.7$ a geometric factor arising from the ellipticity of the magnetic precession [46], and $B_{\text{eff}} = -2K_u^*/M_s$. We neglect the cubic magnetocrystalline anisotropy constant K_1 in the Kerr coefficient as it is small compared to K_u^* in thin-film YIG. The opposite sign of \mathcal{K} in the IP and OOP cases arises from an opposite nonlinearity in the action of the anisotropy field ($\propto -\cos \theta_M$) on the dynamical magnetization (bringing it back to the plane for IP field, or tilting it further away from normal for OOP field), resulting in different directions of Kerr shift as seen in Fig. 2 and Fig. 3. To estimate K_u^* , we fit the magnon resonance field $\mu_0 H_{\text{res}}$ versus θ_H at $f = 11.055 \text{ GHz}$ and obtain $K_u^* = -11.8 \text{ kJ m}^{-3}$ [45], much larger in magnitude than $K_1 = -600 \text{ J m}^{-3}$ in YIG [49]. Using Eq. (3) with $M_s = 144 \text{ kA m}^{-1}$ and $\gamma/(2\pi) = 28 \text{ GHz T}^{-1}$, we obtain $\mathcal{K}_{\text{IP}} = -60.3 \text{ nHz}$ and $\mathcal{K}_{\text{OOP}} = 168.5 \text{ nHz}$, which agrees very well with the experimental values. Notably, these magnon Kerr coefficients are two orders of magnitude larger than those of the smallest YIG spheres, as a result of the smaller magnetic volume and inherently large shape anisotropy of YIG thin films, making them more suitable for inducing nonlinear magnonic phenomena.

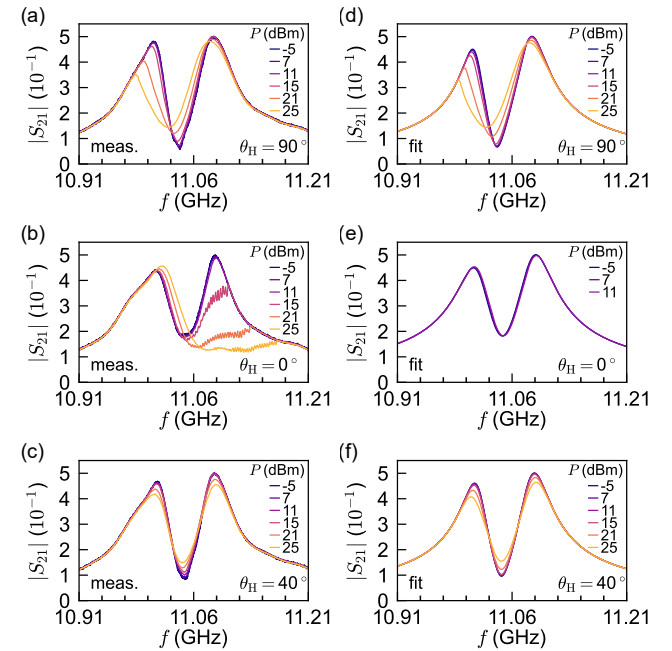


FIG. 3. Power- and frequency-dependent microwave transmission measurements, and fits for the coupled magnon–photon system at a fixed field near the center of the avoided crossing. Field angle is (a,d) $\theta_H = 90^\circ$, (b,e) $\theta_H = 0^\circ$, and (c,f) $\theta_H = 40^\circ$, for (a,b,c) measurements and (d,e,f) fits.

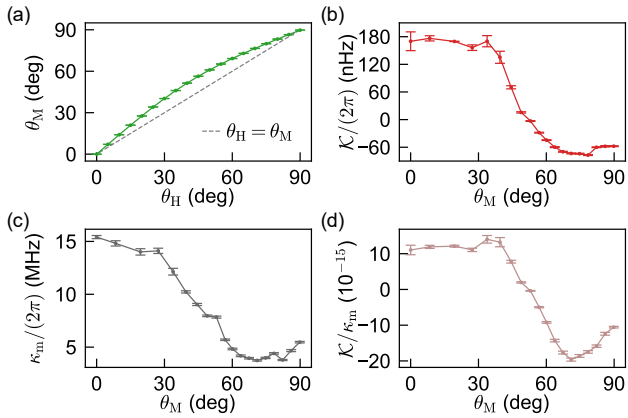


FIG. 4. (a) Dependence of magnetization angle θ_M on field angle θ_H , (b) Kerr coefficient $\mathcal{K}/(2\pi)$, (c) magnon dissipation rate $\kappa_m/(2\pi)$, and (d) anharmonicity defined as \mathcal{K}/κ_m , all as functions of θ_M .

In Fig. 4, we report the complete angle dependence for our measurements. The misalignment of the external and anisotropy fields at intermediate θ_H between IP and OOP directions results in a difference between θ_H and θ_M , with the latter being closer to 90° . We obtain θ_M against θ_H from the angle dependence of the Kittel mode [45] [Fig. 4(a)]. Figure 4(b) shows \mathcal{K} as a function of θ_M and highlights the continuous tunability of \mathcal{K} with magnetization angle. Since the visibility of the Kerr shift depends on the magnitude of \mathcal{K} relative to the magnon dissipation rate κ_m , we use \mathcal{K}/κ_m as our figure of merit for the anharmonicity of the system. The dependence of $\kappa_m/(2\pi)$ on θ_M is shown in Fig. 4(c). Its complex angle dependence has been previously observed in iron garnet thin films, and results from a combination of two-magnon scattering and inhomogeneous broadening effects [51]. This complex behavior extends further into the angle dependence of \mathcal{K}/κ_m , shown in Fig. 4(d). Remarkably, although the Kerr coefficient is largest for OOP magnetization, the largest $|\mathcal{K}|/\kappa_m \sim 2 \times 10^{-14}$ is here obtained neither for IP nor OOP magnetizations but at an intermediate angle near $\theta_M = 70^\circ$.

We compare in Fig. 5 the experimental results for the MKE in our thin-film YIG and YIG spheres from previous studies. Reported values of Kerr coefficient for spheres range in the orders of 0.01 nHz–1 nHz, largely determined by their volume [30–33]. In our extended YIG thin film at room temperature, we obtain up to $\mathcal{K}/(2\pi) = 170$ nHz, which is already two orders of magnitude higher than the smallest spheres, whereas $|\mathcal{K}|/\kappa_m$ is almost comparable, due to the stronger magnon dissipation occurring in thin films (Fig. 5). The detail of the magnetic parameters entering this analysis and further comparison against spheres or patterned thin-film disks with ideal magnetic properties are provided in SM [45].

An important feature is the universality of the MKE deriving from shape anisotropy, which does not de-

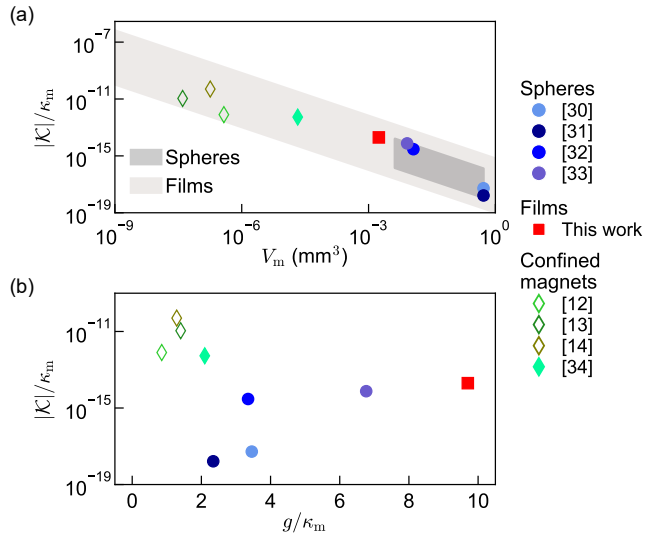


FIG. 5. Experimental observations (filled markers) and extrapolated values based on previous works [12–14, 30–34] (empty markers) for (a) $|\mathcal{K}|/\kappa_m$ versus magnetic volume for spheres and films and (b) anharmonicity $|\mathcal{K}|/\kappa_m$ versus g/κ_m . The shaded region for spheres in (a) represents attainable values of $|\mathcal{K}|/\kappa_m$ calculated for YIG, with $\kappa_m/(2\pi)$ ranging 0.5–25 MHz. For films, the shaded region is both for IP and OOP fields, calculated for YIG and permalloy at $f = 10$ GHz, with $\kappa_m/(2\pi)$ ranging 0.5–500 MHz. We used $M_s = 796$ kA m⁻¹ for permalloy [12].

pend on the magnetic material hosting the magnons or on the temperature of the magnetic system. Indeed, when shape anisotropy dominates over magnetocrystalline anisotropy, $K_u^* = -\mu_0 M_s^2/2$ and Eq. (3) for OOP field yields $\mathcal{K} = \hbar\gamma^2\mu_0/(2V_m)$, a universal parameter that depends only on the sample volume V_m . For IP field, \mathcal{K} is weakly dependent on M_s (and hence also on temperature), through the ellipticity parameter ξ .

Integrated magnon–photon systems comprising a lithographed magnet and a superconducting microwave resonator have been demonstrated to enable strong coupling [12–14]. Although these microscale systems should exhibit large MKE, their nonlinear magnetic behavior has not been reported so far. Based on the present results, we analyze how the MKE is predicted to scale in such systems. We do not treat the nonlinearity of the superconducting resonator and assume the magnetic anisotropy to solely arise from the geometry. Discrete values are presented for Refs. [12–14] in Fig. 5(a), which also includes the range of $|\mathcal{K}|/\kappa_m$ as a function of V_m expected for thin films. Patterned confined magnets allow for a considerable reduction in volume compared to spheres and can easily be as small as $\sim 10^{-9}$ mm³, favoring much stronger $|\mathcal{K}|/\kappa_m$, in addition to sign tunability between IP and OOP fields. Patterning would also mitigate the increase in κ_m due to inhomogeneous broadening in the OOP configuration. Reaching the limit of

$V \sim 10^{-16} \text{ mm}^3$ in YIG, with ~ 5000 spins, would result in $\mathcal{K} \sim \kappa_m$, implementing an effective two-level system [53]. In addition, the MKE in thin films can be further controlled by adjusting magnetic anisotropy stemming from interfacial effects [54, 55], stoichiometry [56–59], strain [51, 60–62], or using antiferromagnets [63, 64].

The trade-off for enhancing the anharmonicity of the magnonic system by reducing its volume is the coherence of the magnon–photon interaction, i.e., the magnon–photon coupling constant g relative to the magnon dissipation rate κ_m . Since $g \sim \sqrt{N}$, the condition $g > \kappa_m$ requires a sufficiently large magnonic system and low magnon dissipation rate. Figure 5(b) shows discrete values of $|\mathcal{K}|/\kappa_m$ versus g/κ_m for YIG spheres and thin films. Our extended film of YIG coupled to the loop-gap resonator provides the largest g/κ_m despite the lower number of spins compared to the spheres.

In summary, we have studied the MKE in a YIG thin film strongly coupled to a microwave resonator at room temperature. We have experimentally demonstrated large magnon Kerr shifts that can be continuously tuned in magnitude and direction by controlling the angle between the film plane and equilibrium magnetization. Our experimental data and theoretical modeling provide a quantitative description of the Kerr coefficients in magnetic thin films, rationalizing the enhancement or suppression of the MKE depending on sample and experimental parameters. The MKE in extended films is two orders of magnitude larger than in YIG spheres. The anharmonicity relative to magnon dissipation is comparable between thin films of standard quality and the best YIG spheres. Extending the present results to micro- or nanopatterned thin-film magnets offers the prospect of stronger and fully tunable nonlinearities, promising compact non-linear cavity-magnonic devices.

ACKNOWLEDGMENTS

This work was supported by the Swiss National Science Foundation (Grant No. 200021- 236524). H.M. acknowledges support from JSPS Postdoctoral Fellowship (Grant No. 23KJ1159), Young Researchers’ Exchange Programme - Special 2023 Call Japan in ETH Zurich, and Swiss Government Excellence Scholarships 2024-2025. H.W. acknowledges the support of the China Scholarship Council (CSC, Grant No. 202206020091). R.S. acknowledges funding by the Deutsche Forschungsgemeinschaft via the SFB 1432, Project No. 425217212. W.L. acknowledges the support of the ETH Zurich Postdoctoral Fellowship Program (21-1 FEL-48) and from a government grant managed by the Agence Nationale de la Recherche as part of the France 2030 program, with reference ANR-24-EXSP-0005 (“MAGNON-BRAQET”).

* davit.petrosyan@mat.ethz.ch

† william.legrand@neel.cnrs.fr

‡ pietro.gambardella@mat.ethz.ch

- [1] O. O. Soykal and M. E. Flatté, Strong field interactions between a nanomagnet and a photonic cavity, *Phys. Rev. Lett.* **104**, 077202 (2010).
- [2] D. Lachance-Quirion, Y. Tabuchi, A. Gloppe, K. Usami, and Y. Nakamura, Hybrid quantum systems based on magnonics, *Appl. Phys. Express* **12**, 070101 (2019).
- [3] Y. Li, W. Zhang, V. Tyberkevych, W.-K. Kwok, A. Hoffmann, and V. Novosad, Hybrid magnonics: Physics, circuits, and applications for coherent information processing, *J. Appl. Phys.* **128**, 130902 (2020).
- [4] B. Zare Rameshti, S. Viola Kusminskiy, J. A. Haigh, K. Usami, D. Lachance-Quirion, Y. Nakamura, C.-M. Hu, H. X. Tang, G. E. Bauer, and Y. M. Blanter, Cavity magnonics, *Phys. Rep.* **979**, 1 (2022).
- [5] Y. Tabuchi, S. Ishino, T. Ishikawa, R. Yamazaki, K. Usami, and Y. Nakamura, Hybridizing ferromagnetic magnons and microwave photons in the quantum limit, *Phys. Rev. Lett.* **113**, 083603 (2014).
- [6] X. Zhang, C.-L. Zou, L. Jiang, and H. X. Tang, Strongly coupled magnons and cavity microwave photons, *Phys. Rev. Lett.* **113**, 156401 (2014).
- [7] A. Gherri, C. Bonizzoni, M. Maksutoglu, A. Mercurio, O. Di Stefano, S. Savasta, and M. Affronte, Ultrastrong magnon-photon coupling achieved by magnetic films in contact with superconducting resonators, *Phys. Rev. Appl.* **20**, 024039 (2023).
- [8] S. Yoshii, M. Müller, R. Ohshima, M. Althammer, Y. Ando, H. Huebl, and M. Shiraishi, On-chip magnon polaritons in the ultrastrong coupling regime (2025), arXiv:2507.06065 [quant-ph].
- [9] H. Huebl, C. W. Zollitsch, J. Lotze, F. Hocke, M. Greifenstein, A. Marx, R. Gross, and S. T. B. Goennenwein, High cooperativity in coupled microwave resonator ferromagnetic insulator hybrids, *Phys. Rev. Lett.* **111**, 127003 (2013).
- [10] L. McKenzie-Sell, J. Xie, C.-M. Lee, J. W. A. Robinson, C. Ciccarelli, and J. A. Haigh, Low-impedance superconducting microwave resonators for strong coupling to small magnetic mode volumes, *Phys. Rev. B* **99**, 140414 (2019).
- [11] R. G. E. Morris, A. F. van Loo, S. Kosen, and A. D. Karenowska, Strong coupling of magnons in a YIG sphere to photons in a planar superconducting resonator in the quantum limit, *Sci. Rep.* **7**, 11511 (2017).
- [12] Y. Li, T. Polakovic, Y.-L. Wang, J. Xu, S. Lendinez, Z. Zhang, J. Ding, T. Khaire, H. Saglam, R. Divan, J. Pearson, W.-K. Kwok, Z. Xiao, V. Novosad, A. Hoffmann, and W. Zhang, Strong coupling between magnons and microwave photons in on-chip ferromagnet-superconductor thin-film devices, *Phys. Rev. Lett.* **123**, 107701 (2019).
- [13] J. T. Hou and L. Liu, Strong coupling between microwave photons and nanomagnet magnons, *Phys. Rev. Lett.* **123**, 107702 (2019).
- [14] S. Guo, D. Russell, J. Lanier, H. Da, P. C. Hammel, and F. Yang, Strong on-chip microwave photon–magnon coupling using ultralow-damping epitaxial $\text{Y}_3\text{Fe}_5\text{O}_{12}$ films at 2 K, *Nano Lett.* **23**, 5055 (2023).

[15] H. Suhl, The theory of ferromagnetic resonance at high signal powers, *J. Phys. Chem. Solids* **1**, 209 (1957).

[16] P. W. Anderson and H. Suhl, Instability in the motion of ferromagnets at high microwave power levels, *Phys. Rev.* **100**, 1788 (1955).

[17] Y. Fetisov, C. Patton, and V. Synogach, Nonlinear ferromagnetic resonance and foldover in yttrium iron garnet thin films-inadequacy of the classical model, *IEEE Trans. Magn.* **35**, 4511 (1999).

[18] D. J. Seagle, S. H. Charap, and J. O. Artman, Foldover in YIG, *J. Appl. Phys.* **57**, 3706 (1985).

[19] E. R. J. Edwards, H. Ulrichs, V. E. Demidov, S. O. Demokritov, and S. Urazhdin, Parametric excitation of magnetization oscillations controlled by pure spin current, *Phys. Rev. B* **86**, 134420 (2012).

[20] T. Brächer, P. Pirro, and B. Hillebrands, Parallel pumping for magnon spintronics: Amplification and manipulation of magnon spin currents on the micron-scale, *Phys. Rep.* **699**, 1 (2017).

[21] T. Makiuchi, T. Hioki, Y. Shimazu, Y. Oikawa, N. Yokoi, S. Daimon, and E. Saitoh, Parametron on magnetic dot: Stable and stochastic operation, *Appl. Phys. Lett.* **118**, 022402 (2021).

[22] V. E. Demidov, O. Dzyapko, S. O. Demokritov, G. A. Melkov, and A. N. Slavin, Thermalization of a parametrically driven magnon gas leading to Bose-Einstein condensation, *Phys. Rev. Lett.* **99**, 037205 (2007).

[23] H. Kurebayashi, O. Dzyapko, V. E. Demidov, D. Fang, A. J. Ferguson, and S. O. Demokritov, Controlled enhancement of spin-current emission by three-magnon splitting, *Nat. Mater.* **10**, 660 (2011).

[24] H. Schultheiss, X. Janssens, M. van Kampen, F. Ciubotaru, S. J. Hermsdoerfer, B. Obry, A. Laraoui, A. A. Serga, L. Lagae, A. N. Slavin, B. Leven, and B. Hillebrands, Direct current control of three magnon scattering processes in spin-valve nanocontacts, *Phys. Rev. Lett.* **103**, 157202 (2009).

[25] O. Lee, K. Yamamoto, M. Umeda, C. W. Zollitsch, M. Elyasi, T. Kikkawa, E. Saitoh, G. E. W. Bauer, and H. Kurebayashi, Nonlinear magnon polaritons, *Phys. Rev. Lett.* **130**, 046703 (2023).

[26] V. T. Synogach, Y. K. Fetisov, C. Mathieu, and C. E. Patton, Ultrashort microwave pulses generated due to three magnon interactions, *Phys. Rev. Lett.* **85**, 2184 (2000).

[27] C. Mathieu, V. T. Synogatch, and C. E. Patton, Brillouin light scattering analysis of three-magnon splitting processes in yttrium iron garnet films, *Phys. Rev. B* **67**, 104402 (2003).

[28] C. L. Ordóñez Romero, B. A. Kalinikos, P. Krivosik, W. Tong, P. Kabos, and C. E. Patton, Three-magnon splitting and confluence processes for spin-wave excitations in yttrium iron garnet films: Wave vector selective Brillouin light scattering measurements and analysis, *Phys. Rev. B* **79**, 144428 (2009).

[29] M. Arfni, A. Bermejillo-Seco, A. Bondarenko, C. A. Potts, Y. M. Blanter, H. S. J. van der Zant, and G. A. Steele, Magnon-magnon interaction induced by nonlinear spin-wave dynamics, *Phys. Rev. Lett.* **135**, 166703 (2025).

[30] Y.-P. Wang, G.-Q. Zhang, D. Zhang, X.-Q. Luo, W. Xiong, S.-P. Wang, T.-F. Li, C.-M. Hu, and J. Q. You, Magnon Kerr effect in a strongly coupled cavity-magnon system, *Phys. Rev. B* **94**, 224410 (2016).

[31] Y.-P. Wang, G.-Q. Zhang, D. Zhang, T.-F. Li, C.-M. Hu, and J. Q. You, Bistability of cavity magnon polaritons, *Phys. Rev. Lett.* **120**, 057202 (2018).

[32] R.-C. Shen, J. Li, Z.-Y. Fan, Y.-P. Wang, and J. Q. You, Mechanical bistability in Kerr-modified cavity magnomechanics, *Phys. Rev. Lett.* **129**, 123601 (2022).

[33] R.-C. Shen, J. Li, Y.-M. Sun, W.-J. Wu, X. Zuo, Y.-P. Wang, S.-Y. Zhu, and J. Q. You, Cavity-magnon polaritons strongly coupled to phonons, *Nat. Commun.* **16**, 5652 (2025).

[34] G.-T. Xu, Z. Shen, M. Zhang, Y. Wang, S. Wan, Y. Yang, T. Zhang, L. Bi, F.-W. Sun, G.-C. Guo, and C.-H. Dong, Kerr-induced synchronization of a broadband magnon-phonon hybrid frequency comb, *Phys. Rev. Lett.* **135**, 203604 (2025).

[35] S.-f. Qi and J. Jing, Kerr-magnon-assisted asymptotic stationary photon-phonon squeezing, *Phys. Rev. A* **111**, 013708 (2025).

[36] Y.-J. Xu, L.-H. Zhai, P. Fu, S.-J. Cheng, and G.-Q. Zhang, Nonreciprocal quantum phase transition in cavity magnonics, *Phys. Rev. A* **110**, 043704 (2024).

[37] V. Bhatt, M. K. Singh, A. B. Bhattacharjee, and P. K. Jha, Magnon blockade based on the magnon Kerr effect in a spinning microwave resonator, *Optik* **327**, 172275 (2025).

[38] J.-L. Tong, Y. Hao, S.-X. Wu, C.-H. Bai, and S. Bai, Nonreciprocal strong mechanical squeezing based on the Kerr effect in cavity-magnon optomechanical system, *Adv. Quantum Technol.* **8**, 2400654 (2025).

[39] C. Kong, H. Xiong, and Y. Wu, Magnon-induced nonreciprocity based on the magnon Kerr effect, *Phys. Rev. Appl.* **12**, 034001 (2019).

[40] Z. Zhang, M. O. Scully, and G. S. Agarwal, Quantum entanglement between two magnon modes via Kerr nonlinearity driven far from equilibrium, *Phys. Rev. Res.* **1**, 023021 (2019).

[41] Q. Guo, J.-X. Wang, C.-H. Bai, Y. Zhang, G. Li, and T. Zhang, Nonreciprocal macroscopic entanglement between two magnon modes induced by Kerr nonlinearity, *Phys. Rev. B* **112**, 144422 (2025).

[42] X.-Y. Ma and J.-L. Guo, Nonreciprocal magnon-magnon entanglement based on magnon Kerr effect, *Opt. Commun.* **587**, 131897 (2025).

[43] Y. Jiang, V. Tyberkevych, Y. Huang, Z. Yan, A. Pishchav, A. Slavin, and X. Zhang, Generation of ultra-broadband frequency comb in strongly bistable nonlinear magnonic resonator (2025), arXiv:2511.22915 [cond-mat.mes-hall].

[44] F. Zanichelli, D. Petrosyan, H. Wang, P. Helbingk, R. Schlitz, P. Gambardella, and W. Legrand, Loop-gap resonators achieving strong magnon-photon coupling in magnetic insulator thin films, submitted.

[45] see Supplemental Material, [URL will be inserted by publisher](#), which presents a list of symbols; fit functions; fit procedure; and fit results at all angles for obtaining the Kerr coefficient, anharmonicity, magnetization angle; the field angle for the onset of two-magnon scattering obtained from MuMax3 simulations; and a comparison of the magnon Kerr coefficient for ideal YIG spheres and YIG thin films, including Refs. [46–50].

[46] D. Petrosyan, H. Matsumoto, H. Wang, R. Schlitz, P. Gambardella, and W. Legrand, manuscript in preparation.

[47] H. Makino and Y. Hidaka, Determination of magnetic anisotropy constants for bubble garnet epitaxial films using field orientation dependence in ferromagnetic resonances, *Mater. Res. Bull.* **16**, 957 (1981).

[48] H. Maier-Flaig, S. Klingler, C. Duba, O. Surzhenko, R. Gross, M. Weiler, H. Huebl, and S. T. B. Goennenwein, Temperature-dependent magnetic damping of yttrium iron garnet spheres, *Phys. Rev. B* **95**, 214423 (2017).

[49] P. Hansen, K. Enke, and G. Winkler, *Part A: Garnets and Perovskites*, edited by K.-H. Hellwege and A. M. Hellwege (Springer-Verlag, 1978).

[50] A. Vansteenkiste, J. Leliaert, M. Dvornik, M. Helsen, F. Garcia-Sanchez, and B. Van Waeyenberge, The design and verification of MuMax3, *AIP Adv.* **4**, 107133 (2014).

[51] L. Soumah, N. Beaulieu, L. Qassym, C. Carrétéro, E. Jacquet, R. Lebourgeois, J. Ben Youssef, P. Bortolotti, V. Cros, and A. Anane, Ultra-low damping insulating magnetic thin films get perpendicular, *Nat. Commun.* **9**, 3355 (2018).

[52] R. Schlitz, L. Siegl, T. Sato, W. Yu, G. E. W. Bauer, H. Huebl, and S. T. B. Goennenwein, Magnetization dynamics affected by phonon pumping, *Phys. Rev. B* **106**, 014407 (2022).

[53] H. Y. Yuan and R. A. Duine, Magnon antibunching in a nanomagnet, *Phys. Rev. B* **102**, 100402 (2020).

[54] A. J. Lee, A. S. Ahmed, B. A. McCullian, S. Guo, M. Zhu, S. Yu, P. M. Woodward, J. Hwang, P. C. Hammel, and F. Yang, Interfacial Rashba-effect-induced anisotropy in nonmagnetic-material–ferrimagnetic-insulator bilayers, *Phys. Rev. Lett.* **124**, 257202 (2020).

[55] B. H. Lee, T. Fakhrul, C. A. Ross, and G. S. D. Beach, Large anomalous frequency shift in perpendicular standing spin wave modes in BiYIG films induced by thin metallic overlayers, *Phys. Rev. Lett.* **130**, 126703 (2023).

[56] D. Scheffler, O. Steuer, S. Zhou, L. Siegl, S. T. B. Goennenwein, and M. Lammel, Aluminium substituted yttrium iron garnet thin films with reduced Curie temperature, *Phys. Rev. Mater.* **7**, 094405 (2023).

[57] A. C. Kaczmarek, E. R. Rosenberg, Y. Song, K. Ye, G. A. Winter, A. N. Penn, R. Gomez-Bombarelli, G. S. D. Beach, and C. A. Ross, Atomic order of rare earth ions in a complex oxide: a path to magnetotaxial anisotropy, *Nat. Commun.* **15**, 5083 (2024).

[58] D. Gouéré, H. Merbouche, A. El Kanj, F. Kohl, C. Carrétéro, I. Boventer, R. Lebrun, P. Bortolotti, V. Cros, J. Ben Youssef, and A. Anane, Temperature-independent ferromagnetic resonance shift in Bi-doped YIG garnets through magnetic anisotropy tuning, *Phys. Rev. Mater.* **6**, 114402 (2022).

[59] W. Legrand, Y. Kemna, S. Schären, H. Wang, D. Petrosyan, L. Holder, R. Schlitz, M. H. Aguirre, M. Lammel, and P. Gambardella, Lattice-tunable substituted iron garnets for low-temperature magnonics, *Adv. Funct. Mater.* **25**, 2503644 (2025).

[60] M. Kubota, K. Shibuya, Y. Tokunaga, F. Kagawa, A. Tsukazaki, Y. Tokura, and M. Kawasaki, Systematic control of stress-induced anisotropy in pseudomorphic iron garnet thin films, *J. Magn. Magn. Mater.* **339**, 63 (2013).

[61] H. Wang, C. Du, P. C. Hammel, and F. Yang, Strain-tunable magnetocrystalline anisotropy in epitaxial $Y_3Fe_5O_{12}$ thin films, *Phys. Rev. B* **89**, 134404 (2014).

[62] T. Fakhrul, B. Khurana, H. T. Nembach, J. M. Shaw, Y. Fan, G. A. Riley, L. Liu, and C. A. Ross, Substrate-dependent anisotropy and damping in epitaxial bismuth yttrium iron garnet thin films, *Adv. Mater. Interfaces* **10**, 2300217 (2023).

[63] I. Boventer, H. T. Simensen, B. Brekke, M. Weides, A. Anane, M. Kläui, A. Brataas, and R. Lebrun, Antiferromagnetic cavity magnon polaritons in collinear and canted phases of hematite, *Phys. Rev. Appl.* **19**, 014071 (2023).

[64] H. Wang, J. Wang, K. Yu, L. Sheng, Y. Zhou, R. Yuan, C. Hua, W. Yu, J. Hu, J. Chen, C. Song, J.-P. Ansermet, M. Elyasi, G. E. W. Bauer, and H. Yu, Long-range propagation of magnon polaritons in a canted antiferromagnet, *Phys. Rev. Appl.* **23**, L061002 (2025).